Relative importance of the mechanisms triggering the Eurasian ice sheet deglaciation

Victor van Aalderen[1], Sylvie Charbit[1], Christophe Dumas[1], and Aurélien Quiquet[1]

[1]Laboratoire des Sciences du Climat et de l'Environnement, LSCE/IPSL, CEA-CNRS-UVSQ, Université Paris-Saclay, 91191 Gif-sur-Yvette cedex, France

Corresponding author: Victor van Aalderen (victor.van-aalderen@lsce.ipsl.fr)

Abstract

The last deglaciation (21000 to 8000 years BP) of the Eurasian ice sheet (EIS), is thought to have been responsible for a sea level rise of about 20 meters. While many studies have examined the timing and rate of the EIS retreat during this period, many questions remain about the key processes that triggered the EIS deglaciation 21,000 years ago. Due to its large marine-based parts in the Barents-Kara and British Isles sectors, EIS is often considered as a potential analog of the current West Antarctic ice sheet (WAIS). Identifying the mechanisms that drove the EIS evolution might provide a better understanding of the processes at play in the West Antarctic destabilization. To investigate the relative impact of key drivers on the EIS destabilization we used the three-dimensional ice sheet model GRISLI (version 2.0) forced by climatic fields from five PMIP3/PMIP4 LGM simulations. In this study, we performed sensitivity experiments to test the response of the simulated Eurasian ice sheets to surface climate, oceanic temperatures (and thus basal melting under floating ice tongues) and sea level perturbations. Our results highlight that the EIS retreat is primarily triggered by atmospheric warming. Increased atmospheric temperatures further amplify the sensitivity of the ice sheets to sub-shelf melting. These results contradict those of previous modelling studies mentioning the central role of basal melting on the deglaciation of the marine-based Barents-Kara ice sheet. However, we argue that the differences with previous works are mainly related to differences in the methodology followed to generate the initial LGM ice sheet. We conclude that being primarily sensitive to the atmospheric forcing, the Eurasian ice sheet cannot be considered as a direct analogue of the present-day West Antarctic ice sheet. However, because of the expected rise in atmospheric temperatures, risk of hydrofracturing is increasing and could ultimately put the WAIS in a configuration similar to the pas Eurasian ice sheet.

1 Introduction

During the last glacial maximum (LGM, 26-19 ka), the Eurasian ice complex was formed by the coalescence of three distinct ice sheets covering the British Isles, Fennoscandia and the Barents and Kara Seas. While the Fennoscandian ice sheet (FIS) was mostly grounded on the bedrock, the British Isles (BIIS) and Barents-Kara (BKIS) were mostly lying below sea level.

The Eurasian ice sheet (EIS) was influenced by various climate regimes with large differences between the western and eastern edges. Due to heat and moisture sources from the North Atlantic current, the British Isles and western Scandinavia were dominated by relatively warm and wet conditions contrasting with the more continental and drier climate in the eastern part of the EIS (Tierney et al., 2020). These various climatic influences prevailing over the three different ice sheets forming the Eurasian ice complex, may have resulted in different responses to variations in atmospheric and oceanic conditions. Over the last decade an active field of research has developed to identify the mechanisms behind the retreat of the Eurasian ice sheet during the last deglaciation, although no clear consensus has yet been reached. According to the recent study of Sejrup et al. (2022) the onset of the northern hemisphere deglaciation was primarily triggered by summer ablation resulting from increased summer insolation at 65 °N, and thus by changes in surface mass balance balance (SMB), defined as the difference between snow/ice accumulation and ablation.

On the other hand, studies based on modeling approaches suggest that the retreat of the marine-based ice sheets could be driven by dynamical processes triggered by the melting of ice shelves (Pattyn et al., 2018). In fact, the relationship between oceanic temperatures and ice sheet mass balance has been confirmed and widely documented for the present-day WAIS. In particular, it has been shown that ocean warming plays a crucial role in accelerating Antarctic mass loss by enhancing basal melting and ice shelf thinning (Pritchard et al., 2012, Konrad et al., 2018, Pattyn et al., 2018; Rignot et al., 2019). This process may trigger a marine ice sheet instability when the bedrock is sloping towards the ice sheet interior. This instability translates into a sustained retreat of the grounding line and a significant glacier acceleration (Schoof, 2012). As large parts of BIIS and BKIS are marine based, their evolution could be driven by sub-shelf melting and potentially by the subsequent marine ice sheet instability. Based on the analysis of benthic and planktic foraminiferal assemblages, ice-rafted debris and radiocarbon dating, Rasmussen and Thomsen (2021) showed that the retreat of the ice in the Svalbard-Barents sector followed the deglacial oceanic, but also atmospheric, temperature changes. Relying on a first-order thermomechanical ice sheet model constrained by a variety of geomorphological, geophysical and geochronological data, Patton et al. (2017) found that the BIIS receded quite quickly in response to moderate increases in surface temperature. By contrast, the BKIS was rather affected by a combination of reduced precipitation and increased rates of iceberg calving. Other modeling studies have attempted to simulate the dynamics of the EIS during the last glacial period and the last deglaciation with the objective of better understanding the evolution of the ice sheet (Petrini et al., 2020; Alvarez-Solas et al., 2019). In a way similar to what is currently observed in West Antarctica, they suggest that large EIS variations are primarily due to the warming of the Atlantic Ocean leading to increased basal melting in the vicinity of the grounding line (Petrini et al., 2020; Alvarez-Solas et al., 2019). However, the models on which these studies are based have no specific treatment for computing ice velocities at the grounding line, making questionable their representation of the grounding line migration.

Because of the diversity of mechanisms that may have influenced the evolution of the three Eurasian ice sheets, the Eurasian ice complex is an interesting case study to investigate the different mechanisms responsible for the ice sheet retreat. As both BKIS and BIIS are marine-based (Svendsen et al., 2004, Gandy et al., 2018, 2021), they are likely to be more sensitive to oceanic temperature variations. Special attention can be given to BKIS because it has often been considered as a potential analogue of the present-day WAIS (Gudlaugsson et al., 2017, Andreassen and Winsborrow, 2009, Mercer, 1970) due to common features such as the ice volume and a bedrock largely grounded below sea level with an upstream deepening (Amante et al., 2009). As a result, in-depth investigations of the BKIS behavior at the LGM can help to better understand the present-day changes and future evolution of West Antarctica.

This wide range of hypotheses regarding the different processes responsible for the EIS destabilization (i.e atmospheric climate, oceanic climate or both) confirms that there is still a lot of unknowns in the EIS dynamics during the last deglaciation and that the debate is not closed. Progress has been made in ice sheet modeling with the development of new generation models computing the full Stocks flow equations. For example, with a refined model resolution near the grounding line, Gandy et al., (2018, 2021) have quantified the impact of oceanic temperatures on the grounding line dynamics and investigated the potential occurrence and effect of the marine ice sheet instability. However, as the computation time is considerably increased, they focus only on specific sectors (i.e. North Sea) and thus do not consider the impact of the other interconnected ice sheets.

In this paper, we present simulations of the entire Eurasian ice complex during the LGM using the three-dimensional GRISLI2.0 (GRenoble Ice Shelf and Land Ice) ice sheet model (Quiquet et al., 2018). GRISLI2.0 includes an explicit calculation of the ice flux at the grounding line derived from the analytical formulation provided by Tsai et al. (2015), which is expected to account for the representation of the marine ice sheet instability. Our ultimate objective is to identify the key mechanisms leading to the EIS deglaciation. Starting from its LGM geometry, we investigate the EIS sensitivity to perturbations of surface air temperature, precipitation rate, basal melting, and sea level to better understand their relative contribution to the EIS destabilization. In this work, the GRISLI2.0 ice sheet model was forced by a panel of ten different climates from the Paleoclimate Modelling Intercomparison Project (PMIP) database (Abe-Ouchi et al., 2015; Kageyama et al., 2021).

The paper is organized as follows. Section 2 provides a description of the basic equations of the GRISLI2.0 ice sheet model. It also includes a presentation of the climate forcing and the experimental setup of the LGM and sensitivity experiments. Section 3 compares our different reconstructions of the EIS at the LGM. The results of the sensitivity experiments are presented in section 4 and discussed in section 5. Concluding remarks are given in section 6.

104

Figure 1: Map of the Eurasian Ice Sheet at the LGM. The white line is the most credible ice extent of the Eurasian
ice sheet at the LGM according to the DATED-1 compilation (Hughes et al., 2016). Dark blue shaded areas
correspond to the location of the main ice streams (Dowdeswell et al., 2016; Stokes and Clark, 2001), and dotted
black lines are delimitations between the Fennoscandian, the Barents-Kara, and the British Isles ice sheets.

2. Model description and experimental set-up

2.1 The GRISLI ice sheet model

In this study, we use the 3D thermomechanical ice sheet model GRISLI2.0 (referred hereafter to as GRISLI) run
on a Cartesian grid with a horizontal resolution of 20 km x 20 km, corresponding to 177 x 257 grid points.

This ice sheet model was initially built to study the Antarctic ice sheet behavior during glacial-interglacial cycles
(Ritz et al. 2001). It was then adapted to the Northern Hemisphere ice sheets (e.g. Peyaud et al., 2007) and tested
under various climatic conditions (Ladant et al., 2014, Le clec'h et al. 2019, Colleoni et al., 2014, Beghin et al.
2014). GRISLI also took part in the Ice Sheet Model Intercomparison Project (ISMIP6) (Goelzer et al.; 2020,
Seroussi et al., 2020, Quiquet and Dumas, 2021a, 2021b) to investigate future sea level changes (Nowicki et al.
2020). A full description of GRISLI can be found in Quiquet et al. (2018). Here, we only remind the basic
principles of the model. The main modification in this new version of GRISLI compared to previous ones (Ritz et

120   al., 2001; Peyaud et al., 2007) is the implementation of analytical formulations of the flux at the grounding line

121   leading to a better representation of the grounding line migration.

122   The evolution of the ice sheet geometry depends on the ice sheet surface mass balance, ice dynamics and isostatic

123   adjustment. Assuming that ice is an incompressible material, changes in ice thickness with time are given by the

124   mass balance equation:

125    $\frac{dH}{dt} = SMB - Bmelt - \nabla(UH)$ (1)

126   with H being the local ice thickness, SMB the surface mass balance, bmelt the basal melting in grounded ice areas

127   and under the ice shelves, U the vertical average velocity, and $\nabla(UH)$ the ice flux divergence.

128   The ice velocity is calculated from the sum of the shallow ice approximation (SIA) and the shallow shelf

129   approximation (SSA) components (Winkelmann et al., 2011). Both approximations take advantage of the small

130   aspect ratio of the ice sheets (Hutter, 1983). The SIA assumes that the longitudinal shear stresses can be neglected

131   compared to the vertical shear stresses and holds for all ice sheet regions where the gravity-driven flow induces a

132   slow motion of the ice (Hutter, 1983). Conversely, the SSA neglects the vertical shear stresses compared to the

133   longitudinal shear stresses, which is generally valid for floating ice shelves (MacAyeal, 1989) and to some extent

134   for fast-flowing ice streams. As a result, the total ice sheet domain can be separated into three regions: floating ice

135   shelves where the ice velocity is computed with the SSA, cold-base areas governed by the SIA, and finally, the

136   temperate-base grounded ice, where the ice velocity is computed as the sum of the SIA and SSA components.

137   The basal friction for the temperate base areas is assumed to follow a linear friction law:

138    $\tau_b = -\beta U_b$ (2)

139   where τ_b is the basal shear stress, U_b the basal velocity and β the basal drag coefficient. The basal drag coefficient

140   depends on the effective water pressure (N), i.e. the difference between water pressure and ice pressure, and on an

141   internal constant parameter ($C_f = 1.5 \ 10^{-6}$ m yr^{-1}):

142    $\beta = C_f N$ (3)

143   At the base of the grounded ice sheet, the basal temperature is also critically dependent on the geothermal heat

144   flux which is given here by the distribution of Shapiro and Ritzwoller (2004).

145   To simulate artificially the effect of ice anisotropy on the ice velocity, most ice sheet models use an enhancement

146   factor in the nonlinear viscous flow law that relates deformation rates and stresses with values generally ranging

147   between 1 and 5. In GRISLI, two enhancement factors are considered (E_{SIA} and E_{SSA}). E_{SIA} is applied to the SIA

148   component of the velocity to increase ($E_{SIA}>1$) the deformation induced by vertical shearing. Conversely E_{SSA} is

149   applied to the SSA component of the velocity to reduce ($E_{SSA}<1$) the deformation due to longitudinal stresses. The

150   model parameters used in this study are the same as those used in Quiquet et al. (2021c) with the exception of E_{SIA}

151   and C_f fixed respectively to 5 (instead of 1.8) and $1.5 \ 10^{-6}$ m yr^{-1} (instead of $1.5 \ 10^{-3}$ m yr^{-1}). Those parameters

152   have been chosen for a better match between the simulated EIS ice volume at the LGM and the geologically-

153   constrained reconstructions (see Section 2.3).

154 The horizontal resolution used in this study is too coarse to simulate explicitly the grounding line migration

155 (Durand et al., 2009). To circumvent this drawback, we use the analytical formulation from Tsai et al. (2015), in

156 which the ice flux at the grounding line is computed as a function of the ice thickness and a backforce coefficient

157 accounting for the buttressing effect of the ice shelves. In this way, a flow at the grounding line can be simulated

158 with a lower resolution allowing time saving in the simulations. Technical details on this implementation in the

159 GRISLI model are given in Quiquet et al. (2018).

160 At the ice shelf front, calving is computed using a simple ice thickness criterion by prescribing a minimal ice

161 thickness set to 250 m below which ice is calved.

162 2.2 Climate forcing

163 We forced GRISLI with the absolute climatic fields from general circulation model (GCM) outputs of the

164 PMIP3/PMIP4 database (Kageyama et al., 2021). All the GCMs for which LGM simulations were available at the

165 time of writing the manuscript have been selected (see Table 1).

166 Monthly surface air temperatures and solid monthly precipitation are used to compute the surface mass balance

167 defined as the difference between snow/ice accumulation and ablation. Ablation is calculated using a positive

168 degree-day (PDD) method following the formulation of Tarasov and Peltier (2002). Snow accumulation is

169 calculated from the total precipitation (rain and snow), considering only months where monthly temperatures are

170 under the melting point.

171 Due to the differences between GCM and GRISLI resolutions, the GCM outputs are bi-linearly interpolated onto

172 the ice sheet model grid. In addition, to account for orography differences between GRISLI and the GCMs, the

173 surface air temperatures of the GCMs are corrected using a constant vertical temperature gradient $\lambda = 7$ °C km^{-1}:

174 $$T(t)_{GRISLI} = T_{GCM}^{LGM} - \lambda(S(t) - S_{GCM}^{LGM}) \qquad (4)$$

175 where $T(t)_{GRISLI}$ is the time-dependent surface air temperature at the surface elevation $S(t)$ simulated by the ice

176 sheet model, and T_{GCM}^{LGM} and S_{GCM}^{LGM} are the LGM surface air temperature and orography computed by the GCMs.

177 This temperature correction induces a change in precipitation which is computed following the Clausius-Clapeyron

178 formulation for an ideal gas:

179 $$pr(t)_{GRISLI} = pr_{GCM}^{LGM} * \exp(\omega * (T(t)_{GRISLI} - T_{GCM}^{LGM})) \quad (5)$$

180 where $pr(t)_{GRISLI}$ is the precipitation calculated by GRISLI at each time step and pr_{GCM}^{LGM} is the LGM precipitation

181 computed by the GCM and interpolated on the GRISLI grid. ω is the precipitation ratio to temperature change and

182 is fixed to 0.11 °C^{-1} (Quiquet et al., 2013).

183 Following DeConto and Pollard (2012), the sub-shelf melt rate (OM) is computed using ocean temperature and

184 salinity:

185 $$OM = K_t \frac{\rho_w C_w}{\rho_i L_f} |T_o - T_f| (T_o - T_f) \quad (6)$$

186 where K_t is called the transfer factor and is set to 7 m yr^{-1} °C^{-1} in the baseline experiments as in DeConto and

187 Pollard (2012), ρ_w the ocean water density, ρ_i ice density, L_f the latent heat of ice fusion, C_w the specific heat of

188   ocean water and T_o is the local ocean temperature. T_f is the local freezing point temperature, depending on the

189   ocean salinity (S) and computed by the Beckmann and Goosse (2003) parameterization:

190   $T_f = 0.0939°C - S \times 0.057°C + z \times 7.6410^{-4}°C$ (7)

191   where z is the ocean depth.

192   A difficulty related to the oceanic forcing fields is that the GCMs do not provide any oceanic information outside

193   their land-sea mask and under the ice shelves. To fill these gaps, we performed a classical near neighbour horizontal

194   extrapolation of temperature and salinity except that we perform this extrapolation within 10 sectors

195   independently. These sectors roughly correspond to drainage basins (Fig. S1). The definition of these basins is

196   based on bedrock topographic features and LGM ice elevation and is somehow comparable to the approach

197   followed by Zwally et al. (2015) for Antarctica. The horizontal extrapolation is performed for each individual

198   vertical layer, without any vertical interpolation. This extrapolation method provides information on temperature

199   and salinity within the entire ice shelf cavity for each vertical level of the GCMs. These temperature and salinity

200   fields are then used to compute the sub-shelf melt rate (Eq. 6), using a linear vertical interpolation between the two

201   oceanic layers bounding the ice shelf depth. The only exception is when the PMIP3/PMIP4 simulations do not

202   provide data in a given sector. In this case, a constant and homogeneous basal melting value of 0.1 m yr^{-1} is

203   prescribed. This mainly occurs in the continental southern flanks of the Eurasian ice sheet.

204   In GRISLI, each grid point can either be a floating or a grounded ice point. To account for the fact that the sub-

205   shelf melt rate is higher in the vicinity of the grounded line (Beckmann and Goose, 2003) and due to the coarse

206   resolution of the model, we apply a fraction of the neighbouring floating sub-shelf melt rate to the last grounded

207   point as in De Conto and Pollard (2012). This approach allows to take the potential influence of the ocean into

208   account.

209   **Table 1:** PMIP3 and PMIP4 models used to force GRISLI. The fourth column indicates the choice of the ice sheet

210   boundary condition at the LGM for each GCM simulation. ice sheet reconstructions used as a boundary condition

211   of the GCM simulations at the LGM.

model	References	PMIP/CMIP	Boundary condition
MPI-ESM-P	Adloff et al. (2018)	CMIP5 PMIP3	PMIP3 ice sheet
MRI-CGM3	Yukimoto S et al. (2012)	CMIP5 PMIP3	PMIP3 ice sheet
MIROC-ESM	Sueyoshi et al. (2013)	CMIP5 PMIP3	PMIP3 ice sheet
CNRM-CM5	Voldoire et al. (2013)	CMIP5 PMIP3	PMIP3 ice sheet
GISS-E2-R	Ullman et al. (2014)	CMIP5 PMIP3	PMIP3 ice sheet
FGOALS-g2	Zheng and Yu (2014)	CMIP5 PMIP3	PMIP3 ice sheet
IPSL-CM5A-LR	Dufresne et al. (2013)	CMIP5 PMIP3	PMIP3 ice sheet
IPSL-CM5A2	Sepulchre et al. (2020)	CMIP6 PMIP4	ICE-6G_C
MIROC-ES2L	Hajima et al. (2020)	CMIP6 PMIP4	ICE-6G_C
MPI-ESM1.2	Mauritsen et al. (2019)	CMIP6 PMIP4	ICE-6G_C

2.3 LGM equilibrium

As mentioned above, the main objective of the present paper is to investigate the mechanisms responsible for the EIS retreat from its LGM configuration. To do this, a preliminary step is to build the EIS at the LGM.

We performed ten 100 000-years spin-up experiments (one for each GCM) forced by a constant LGM climate provided by the ten GCMs. Simulations start with no ice sheet and the eustatic sea level is prescribed at 120 m below the present level. The initial bedrock topography corresponds to the present-day topography from ETOPO1 (Amante et al., 2009). This procedure is required to obtain internal ice sheet conditions in equilibrium with the climate forcing and to examine whether the LGM climate can build and maintain the EIS when it is used as input to the GRISLI ice sheet model. From this climate forcing ensemble, we only selected those leading to LGM ice sheets in a reasonable agreement with the most credible ice extent in the DATED-1 database (Hughes et al., 2016) and with the geologically-constrained ice thickness reconstructions, namely ICE-6G_C (Peltier et al., 2015), GLAC-1D (Briggs et al., 2014; Tarasov et al., 2012; Tarasov and Peltier, 2002), and ANU (Lambeck et al., 1995, 1996, 2010).

2.4 Sensitivity experiments

To quantify the relative importance of the three main drivers (i.e., surface mass balance, sub-shelf melt rate, and sea level) of the EIS retreat, we applied time-constant perturbations on the atmospheric and oceanic GCM forcings, and we changed the prescribed sea level. The perturbed simulations are run for 10000 years. We analysed the response at year 1000 of the simulation to investigate the impacts of climate changes that may have occurred at the beginning of the deglaciation and at year 10,000 to examine the sensitivity of EIS on longer time scales.

In the first series of experiments (EXP1), we investigate the effect of SMB changes by increasing surface air temperatures. During the last deglaciation (21 – 8 ka), the mean annual global surface air temperature increased by $4,5° \pm 0.9°$ (Annan et al., 2022). In order to simulate a range of anomalies representative of the onset of the last deglaciation, we chose to apply perturbations from 1 to 5 °C to the mean annual GCM forcing fields, without accounting for related changes in precipitation (see Eq 5). The increase in precipitation in response to increased temperatures (Eq. 5) is considered in the second set of experiments (EXP2).

The third series of experiments (EXP3) is designed to assess the role of oceanic forcing on the EIS stability. Because the basal melting below the ice shelves depends linearly on the Kt transfer coefficient and is a quadratic function of the oceanic temperatures, we performed two sub-series of experiments by modifying either the Kt values (EXP3.1) without modifying the oceanic temperatures, or by applying perturbations to the oceanic temperatures (EXP3.2). Observations below the Antarctic ice shelves show that the basal melting rate ranges from 0 to 35 m yr^{-1} for oceanic temperatures between -2 °C and 2 °C (Holland et al., 2008). This wide range of basal melting rate values reflects the complexity of such a process that can only be partially represented with simple parameterizations (Eq. 6). The Kt coefficient is thus largely uncertain. Therefore, to investigate changes in the EIS sensitivity to the amplitude of basal melting, we first use a wide range of values for this transfer coefficient, i.e. between 10 and 50 m yr^{-1}°C^{-1}.

The mean global sea surface temperature anomaly inferred from the MARGO project (MARGO project members, 2009) between the Late Holocene and the LGM is 1.9 ±1.8°C consistent with the findings (~2.7°C) of Tierney et

249   al. (2020). In the early phase of the deglaciation, the ocean warming was probably less than that of the Late

250   Holocene. Therefore, for the EXP3.2 experiments, we first apply perturbations of 0.5°C, 1.0°C, 1.5°C to the

251   oceanic temperatures (same perturbation on all vertical levels) and we fix the Kt coefficient to 7 m °C^{-1} yr^{-1}. In the

252   transient simulation of the last deglaciation performed by Liu et al. (2009), large increases in oceanic temperatures

253   are obtained. For example, a +9°C warming is obtained in the BJR sector at 500-600 m ocean depth and almost

254   7.5°C in the SA sector at 400-500 m. To reproduce the large increase in the subsurface ocean temperature obtained

255   in Liu et al. (2009), we performed additional sensitivity experiments with perturbations of 7.5°C and 10°C applied

256   in the entire oceanic column.

257   Atmospheric and oceanic temperatures are the two main factors potentially responsible for the destabilization of

258   marine ice sheets. Thus, the fourth series of experiments (EXP4) combines surface air temperature perturbations

259   (ΔT = +2°C, +3°C, and +4°C) with basal melting rate perturbations (Kt = 10, 15 and 25 m yr^{-1} °C^{-1}).

260   Finally, in the fifth set of experiments (EXP5), we also explore the EIS sensitivity to sea level. Indeed, sea level

261   rise favors the retreat of the grounding line and is therefore another potential driver of the MISI. At the beginning

262   of the deglaciation, the global sea level increased by more than 10 m (Carlson and Clark, 2012) raising the global

263   sea level from -120 m to -110 m compared to the present-day eustatic sea level. This abrupt change may have

264   played an important role in the destabilisation of the ice sheet. On the other hand, Gowan et al., (2021) shows that

265   the local sea level around the EIS margin displays a significant spread at the LGM, from -70 m to -140 m,

266   compared to the present-day level and can abruptly change in response to variations in the land-ice mass

267   distribution. Consequently, to better explore the EIS sensitivity to both global mean sea level and local sea level

268   at the beginning of the last deglaciation, we apply moderate (-115 m, -110 m, and -105 m) and large (-90 m, -60 m,

269   -30 m, and 0 m) sea level perturbations with respect to the present day.

270   **3. Available ice sheet reconstructions and ice streams signature**

271   **3.1 Ice sheet geometry**

272   The DATED-1 database is based on evidence found in the existing literature and retrieved from various geological

273   materials (e.g., terrestrial plant macrofossils, foraminifera, speleothems, bones…) analyzed with a range of dating

274   methods. Based on these data, the DATED-1 compilation provides three different scenarios for the maximal,

275   minimal and most credible EIS extent. The GLAC-1D, ICE-6G_C, and ANU reconstructions are based on inverse

276   modeling approaches constrained by GPS data, relative sea level and geomorphological data.

277   The main differences in the three DATED-1 scenarios at the LGM (Hughes et al., 2016) are related to the potential

278   BIIS-FIS connection (or disconnection), the southern continental limit of the FIS and the eastern limit of BKIS

279   (Fig. 2a). Only the minimum scenario suggests the absence of ice between the BIIS and FIS.

280   The GLAC-1D reconstruction agrees well with the most credible DATED-1 scenario, despite a slightly greater ice

281   extent in most of the Fennoscandian regions and a smaller extent in the Taymyr Peninsula (in the easternmost part

282   of the BKIS, Fig. 2d). This contrasts with the ANU and ICE-6G_C reconstructions whose ice limit goes beyond

283   that of the most credible DATED-1 scenario.

284   The differences between the three geologically-constrained reconstructions are due to differences in the inverse

285   methods used to estimate the ice thickness, to the geological and geomorphological data considered to infer the

286 ice extent, and to different choices regarding the Earth rheology. This translates into differences in the altitude of
287 the EIS. For example, in the ANU and GLAC-1D reconstructions, the FIS peaks at 3000-3500 m, while BKIS
288 does not exceed 2500 m (2000 m for GLAC-1D). By contrast, ICE-6G_C provides a larger ice thickness over the
289 BKIS sector (2500-3000 m) than over Fennoscandia.
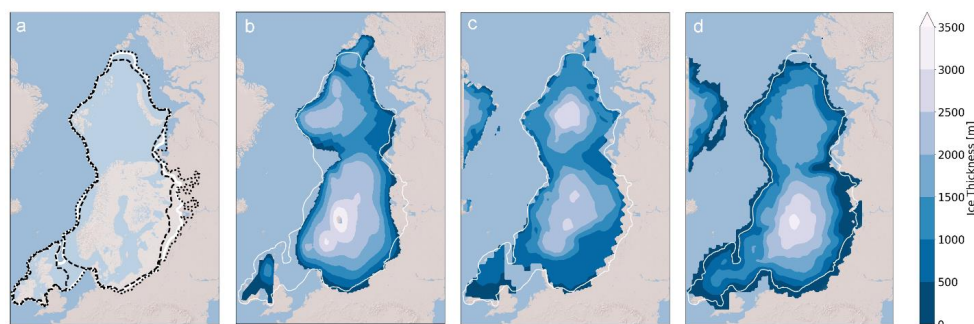
290

291 **Figure 2:** a/ Ice sheet extent at the LGM derived from the DATED-1 compilation (Hughes et al., 2016). The
292 maximum and the minimum scenarios of the ice extent are represented by the dotted and the dashed lines
293 respectively. b/ Ice thickness at the LGM provided by the ANU reconstruction (Lambeck et al., 1995, 1996, 2010;
294 Abe-Ouchi et al., 2015). c/ Same as b/ for the ICE-6G_C reconstruction (Peltier et al., 2015). d/ Same as b/ for the
295 GLAC-1D reconstruction (Briggs et al., 2014; Tarasov et al., 2012; Tarasov and Peltier, 2002). In the four panels,
296 the white line corresponds to the most credible scenario of the ice extent at the LGM derived from the DATED-1
297 compilation (Hughes et al., 2016).

298 **3.2 Ice stream signature**

299 Ice streams also play a key role in ice sheet dynamics and in featuring ice sheet geometry (Pritchard et al., 2009).
300 It is therefore crucial that the dynamics of the simulated ice sheets is consistent with reconstructions. The signature
301 of ice streams can be inferred from geomorphological observations in the Barents Sea, in particular those of the
302 Bjornoyrenna (BJR) and Svyataya Anna (SA) ice streams (Fig. 1) (Polyak et al., 1997; Andreassen and
303 Winsborrow, 2009; Dowdeswell et al., 2016,2021; Szuman et al., 2021). Other geomorphological observations
304 strongly suggest the existence of paleo ice streams in the FIS, such as the Mid-Norwegian (MN) ice stream (Stokes
305 and Clark, 2001), and the Norwegian Channel (NC) ice stream between the FIS and BIIS (Sejrup et al., 1994;
306 Svendsen et al., 2015; Stokes and Clark, 2001).

307 **4. Results**

308 **4.1 LGM equilibrium**

309 At the end of the 100 000-year spin-up simulations, a wide range of ice sheet geometries is obtained (Fig. 3).
310 Simulations performed with CNRM-CM5, MRI-CGM3 and MIROC-ES2L do not succeed in building an ice sheet
311 over Eurasia.

312 This is primarily explained by high positive summer surface air temperatures simulated by the three models in
313 most parts of the EIS compared to the other models, with temperature anomalies ranging between +4.7°C and

314   +11.7°C (Fig. 4). Conversely, with the GISS-E2-R and FGOALS-g2 models, significant ice thickness is built east

315   and south of BKIS because of strong negative mean summer temperatures in this area (Fig. 4).

316   Therefore, we discarded these models and only selected those (MPI-ESM-P, MIROC-ESM, IPSL-CM5A2, IPSL-

317   CM5-LR, and MPI-ESM1.2) providing ice sheet geometries in a relatively good agreement with the

318   reconstructions.

319   The five selected ice sheets do not show significant differences (Fig 3). The FIS peaks at 2500-3000 m, while the

320   BKIS is lower (2000 – 2500 m) due to a drier atmosphere compared to that overlying the Fennoscandian region

321   (Fig. 5). The simulated FIS agrees with the ICE-6G_C reconstruction despite a flatter dome simulated with MPI-

322   ESM-P, about 500 m lower compared to GLAC-1D and ANU. Conversely, the BKIS maximum altitude simulated

323   by GRISLI is underestimated compared to ICE-6G_C while it is in good agreement with the two other

324   reconstructions. The BKIS margins bordering the Greenland and Norwegian Seas and the Arctic Ocean generally

325   match with the most credible DATED-1 scenario of the ice extent. However, in the five GRISLI simulations, the

326   ice extent is too large in the eastern and southern edges compared to DATED-1.

327   The most likely cause of this mismatch is related to the imprint of the ice sheet reconstructions used as boundary

328   conditions of GCM simulations. Indeed, both the ice sheet reconstruction used for PMIP3 simulations (not shown)

329   and ICE-6G_C (Fig. 2c) used in PMIP4 runs overestimate the ice extent in the region of the Taimyr Peninsula.

330   This results in an enhanced cooling favoring the simulated ice expansion in this area. This effect can be amplified

331   by the projections of the ice sheet reconstructions on the coarser GCM grid that may produce an artificial spread

332   of the ice sheet mask, causing further a too extended cooling. Another source of disagreement between DATED-

333   1 and the simulated ice sheets can be due to the representation the jet stream and planetary waves in the coarse

334   resolution climate models, such as the PMIP models. Indeed, such large-scale atmospheric features directly impact

335   the simulated precipitation and temperatures and may cause too much precipitation or too much cooling if

336   improperly represented (Löfverström and Liakka, 2018).
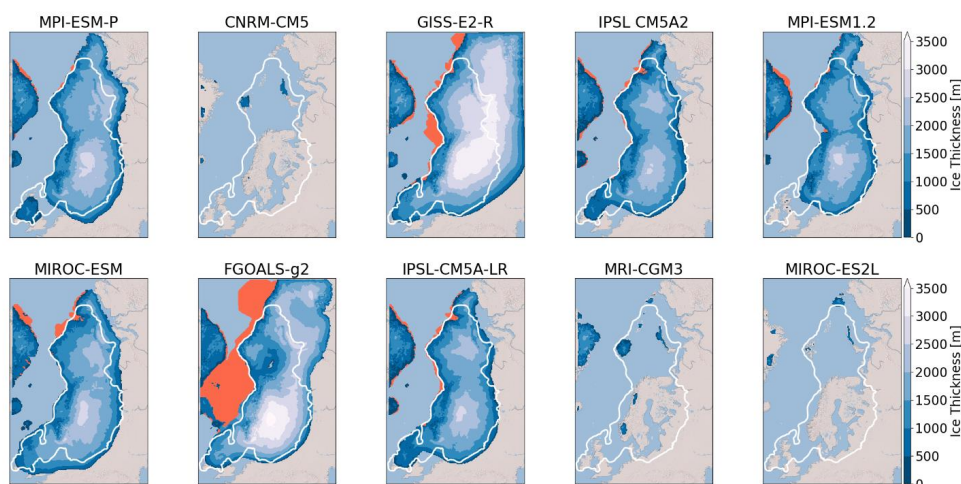
337

338   **Figure 3:** Ice thickness at the end of the 100 000-year simulation for the different GCMs used as forcing of the

339   GRISLI ice sheet model. The white line is the most credible extent derived from the DATED-1 compilation and

340   the orange shaded areas are the simulated ice shelves.

341   For the five selected GCMs, areas with high ice velocities are simulated in the BKIS region (Fig. 6). The highest

342   velocities are obtained for the SA, BJR, NC and MN ice streams and can exceed 1000 m yr^{-1}. In addition, the BJR

343   ice stream shows a large extension from the center of BKIS, with velocities between 75 to 200 m yr^{-1}, to the edge

344   of BKIS. The location of the main fast flowing areas is consistent with empirical evidence based on observations

345   of submarine landforms (Dowdeswell et al., 2016; Stokes and Clark, 2001). It is also interesting to mention that

346   ice velocities of similar magnitude in the present-day Antarctic and Greenland ice sheets have been revealed thanks

347   to radar observations (Solgaard et al., 2021; Mouginot et al., 2019).

348   Overall, our five remaining simulated ice sheets show a reasonable agreement with the different reconstructions

349   constrained by geological and geomorphological observations, both in terms of ice extent and ice thickness as well

350   as dynamical characteristics. The observed differences with the reconstructions remain within the range of

351   uncertainties, which is itself illustrated by the differences between the three reconstructions GLAC-1D, ANU and

352   ICE-6G_C and by the three ice extent scenarios from the DATED-1 compilation.

353   This allows us to use the five spin-up GRISLI experiments (forced by MPI-ESM-P, MIROC-ESM, IPSL-CM5A2,

354   IPSL-CM5-LR, and MPI-ESM1.2) as a starting point to test the sensitivity of the EIS to atmospheric, oceanic and

355   sea level forcings.
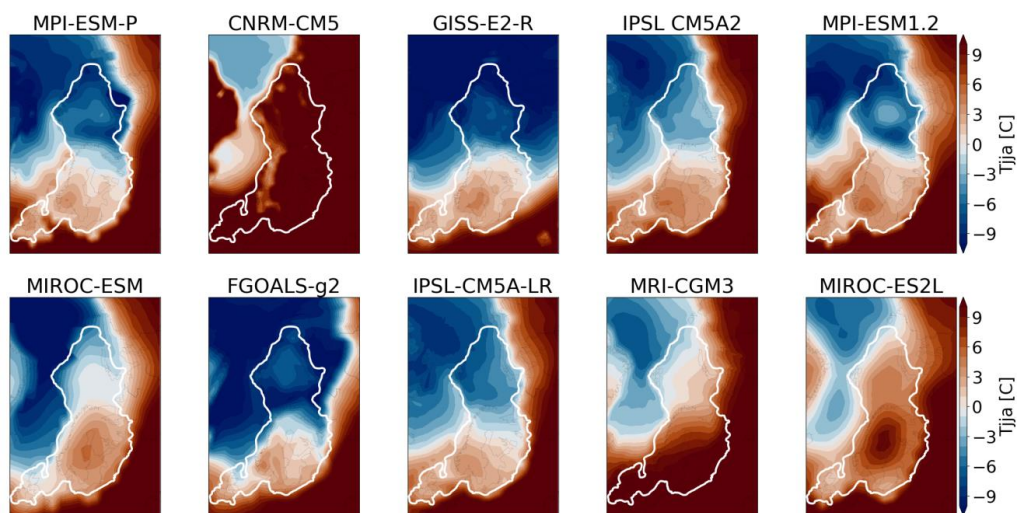
356

357   **Figure 4:** Mean summer (JJA) surface air temperature at 21 ka simulated by each GCM at the sea level and

358   interpolated on the GRISLI grid. The white line represents the ice extent as defined by the most credible DATED-

359   1 scenario.
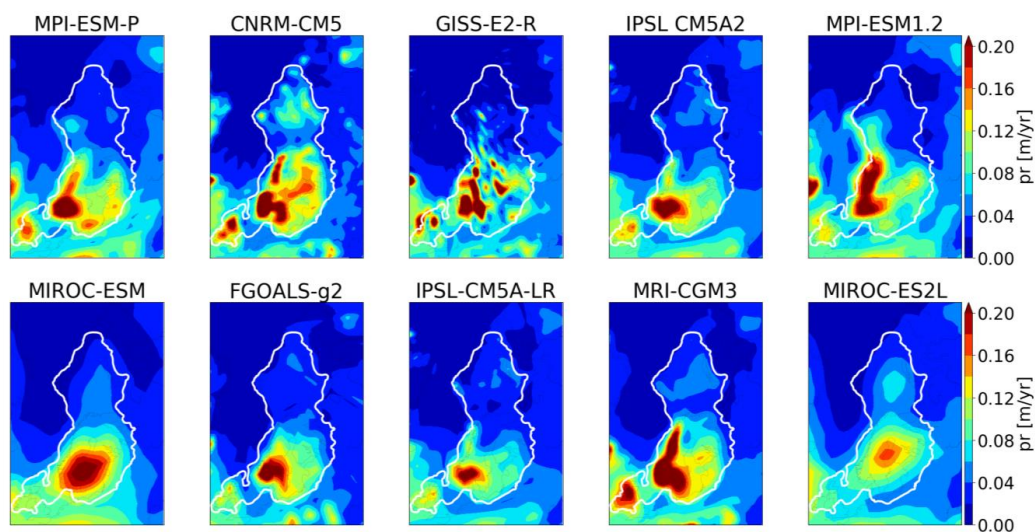
Figure 5: Same as Figure 4 for the mean annual precipitation.
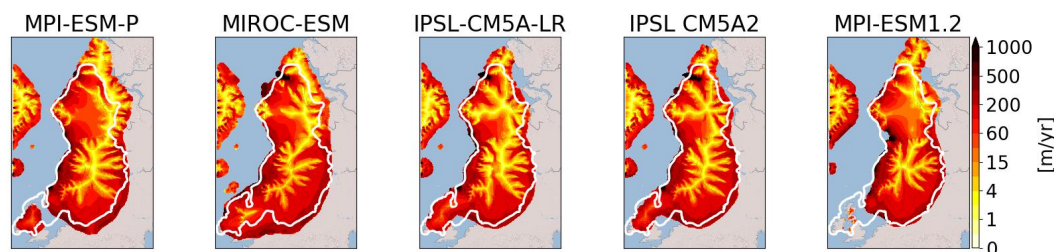
Figure 6: Simulated ice velocities at the end of the 100 000-year LGM simulation. The solid white line represents the most credible ice extent from the DATED-1 compilation.

4.2. Sensitivity experiments

In the following, we investigate the sensitivity of the Eurasian ice sheet to the potential drivers of ice sheet retreat: atmospheric changes responsible for SMB changes (i.e., temperature and snow accumulation to the first order), oceanic changes (sub-shelf melt rate) and sea level changes.

4.2.1 EXP1: Surface air temperature

The aim of this section is to investigate the sensitivity of EIS to a temperature rise. For each temperature perturbation (T_{add} = 1 to 5°C) applied uniformly on the monthly mean surface air temperatures, Figure 7 displays for the multi-model mean the percentage of the ice thickness lost after 1000 years with respect to the initial configuration. The results are plotted for the largest ice sheet mask. This mask corresponds to all areas where ice has been simulated in at least one of the 5 simulations. This means that multi-model means are computed with 1, 2, 3, 4 or 5 models involved, depending on the ice sheet mask of each individual model.

376   For T_{add} = 1 °C, the response of the Eurasian ice sheets is weak, except for the British Isles sector (Fig 7) for which

377   mean JJA temperatures of the five selected GCMs are close to the melting point (Fig. 4). Substantial ice losses are

378   also simulated in the FIS margins for temperature rise greater than 1 °C leading to a progressive retreat of the edge

379   of the ice sheet as the temperature increases. The sensitivity of the BIIS and FIS regions to these temperature

380   perturbations is explained by a shift from positive to negative SMB values when temperature increases (Fig. SP2).

381   By contrast, as the BKIS is located in colder areas, larger temperature perturbations (3 to 5 °C) are necessary to

382   initiate the ice sheet's retreat. The southern BKIS margin appears the most sensitive region, followed by the region

383   of the SA ice stream. In the SA sector, ice thickness losses between 30 % (Tadd = +3°C) to 50 % (Tadd = +5°C)

384   are obtained. In the BJR sector, ice losses are only simulated for large temperature perturbations.

385   However, it is worth mentioning that for a given temperature perturbation, significant differences in the behavior

386   of the five simulated ice sheets can be observed. To illustrate these differences, we plotted for each simulation, the

387   percentage of the ice thickness lost after 1000 years with respect to the initial configuration (Fig SP3). The most

388   sensitive regions to surface air temperature, namely the FIS margins and the SA/BJR sectors, are the locations

389   where inter-model differences in ice thickness losses are the most significant and are amplified with temperature

390   increase. In the BJR sector, the retreat of the ice sheet is simulated for perturbations of 4°C with three GCM

391   forcings (MIROC-ESM, IPSL-CM5A-LR and IPSL-CM5A2, Fig SP3), while this sector is stable with the two

392   other forcings (MPI-ESM-P and MPI-ESM1.2) under this temperature perturbation. In the SA sector, the MIROC-

393   ESM-P forcing produces a retreat from a temperature anomaly of 2°C, but for the IPSL-CM5A-LR and IPSL-

394   CM5A2 forcings the retreat is only triggered for T_{add} = 3 °C. By contrast, the two versions of the MPI-ESM

395   produce a more stable ice sheet in the SA sector since, even with a 5 °C temperature perturbation, the ice retreat

396   is not triggered within the 1000 years of simulation.

397   The lower sensitivity of BJR sector, compared to the SA sector, can be explained (at least partly) by the topography

398   differences between these two regions. Actually, the initial topography of each GCM (not shown) exhibits a trough

399   in the SA sector which does not appear in the region of the BJR ice stream. The lower surface topography in the

400   SA sector is accompanied by higher surface temperatures and thus to larger ice losses when temperature

401   perturbations are applied (Fig. SP3). Moreover, the difference in the sensitivity of the BJR and SA sectors can be

402   also explained by the higher precipitation rate in the BJR sector (between 0.2 to 0.5 m yr^{-1} for the BJR ice stream

403   and less than 0.2 m yr^{-1} for the SA sector, Fig. 5), which can partly counteract the effect of temperature increase

404   on ice mass loss.
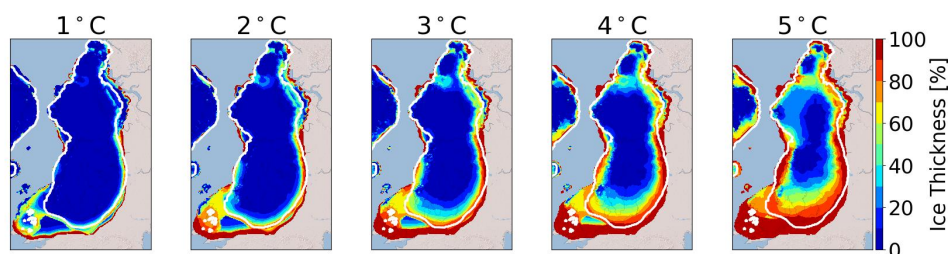
405

406   **Figure 7:** Multi-model mean of the ice thickness lost after 1000 GRISLI model years in the EXP1 experiments

407   with respect to the ice thickness of the LGM ice sheet (red: 100% lost). The results are plotted on the largest ice

408   sheet mask. The white line corresponds to the common ice sheet mask of the five models, i.e., where the multi-

409   model mean is computed on the 5 models.

410   To better understand the effect of precipitation on the EIS stability, the EXP2 combines the precipitation and

411   surface air temperature perturbations. The results obtained in the EXP2 experiments are shown in figure SP4. For

412   BIIS and FIS, a similar behavior to EXP1 is observed, albeit with less ice melt due to increased accumulation as a

413   result of increased temperatures. On the contrary, in EXP2, a large difference with EXP1 is simulated for BKIS,

414   where only the ice sheet margins show sensitivity to increased temperature and precipitation. While an inland ice

415   loss between 20% and 50% was simulated in EXP1 in some places, it is generally limited to less than 10% in

416   EXP2. This result shows the significant role of precipitation to counteract the ice loss due to an increase in surface

417   air temperature.

418   4.2.2 EXP3: Basal melting

419   Besides changes in SMB, another factor that can destabilize a marine ice sheet is the basal melting under the ice

420   shelves (Pritchard et al., 2012). In the LGM experiments, the numerical K_t value is fixed to 7 m °C^{-1} yr^{-1} and leads

421   to basal melting rates in the BJR and SA sectors of 3.1 m yr^{-1} and 0.7 m yr^{-1} respectively. To investigate the effect

422   of increased basal melting that likely occurred during the last deglaciation as a response of increased ocean

423   temperatures, we performed sensitivity experiments by first changing the K_t value (EXP3.1). The sensitivity to

424   oceanic temperatures (EXP3.2) will be discussed later.

425   Figure 8 displays the percentage of ice thickness losses (with respect to the initial configuration) for K_t ranging

426   from 10 m °C^{-1} yr^{-1} to 50 m °C^{-1} yr^{-1}. After 1000 years of simulation, no change in ice thickness is observed for K_t

427   = 10 m°C^{-1} yr^{-1}. For higher K_t values (15 m °C^{-1} yr^{-1} and 25 m °C^{-1} yr^{-1}), ice losses between 30% to 40% are

428   simulated in the MN ice stream sector, and 100% of the ice shelf in the south of SA sector is melted (see Fig 3

429   showing the presence of ice shelves at the end of the spin-up experiment). This corresponds to basal melting rates

430   (multi-model mean) near the grounding line ranging from 7.5 m yr^{-1} (K_t = 15 m °C^{-1} yr^{-1}) to 10.4 m yr^{-1} (K_t = 25

431   m °C^{-1} yr^{-1}) in the MN sector and from 1.7 m yr^{-1} (K_t = 15 m °C^{-1} yr^{-1}) to 2.9 m yr^{-1} (K_t = 25 m °C^{-1} yr^{-1}) in the SA

432   sector. However, these changes are restricted to small areas, and the ice loss is not significant enough to firmly

433   indicate a noticeable sensitivity to basal melting. Perturbations with K_t values above 25 m °C^{-1} yr^{-1} are necessary

434   to observe significant changes in the EIS configuration. In particular, for K_t = 50 m °C^{-1} yr^{-1}, the ice is entirely

435   melted near the BIIS margins, and less than 50 % of the ice remains in the regions of MN, SA and BJR ice streams.

436   Nonetheless, only the simulations forced by MPI-ESM-P, MPI-ESM1.2 and MIROC-ESM show a sensitivity to

437   basal melting in BJR, MN and SA sectors (Fig. SP5). Depending on the GCM forcing, the simulated basal melting

438   values range between 25.7 and 28.7 m yr^{-1}, 24.4 and 28.2 m yr^{-1} and between 11.2 and 13.4 m yr^{-1} for the BJR,

439   MN and SA sectors respectively. By contrast, very small values are obtained with IPSL-CM5A2 (0.2 m yr^{-1} 0.5 m

440   yr^{-1}) and IPSL-CM5A-LR models (0.5 m yr^{-1}). This can be explained by the cold oceanic temperatures near the

441   BJR sector compared to those simulated by the three other GCMs (Fig SP6). These results show that the basal

442   melting has the ability to destabilize the BKIS when it exceeds a certain threshold. Results inferred from the

443   simulations forced by MPI-ESM-P, MPI-ESM1.2 and MIROC-ESM suggest that this threshold is obtained for K_t

444   values between 25 and 50 m °C^{-1} yr^{-1}, corresponding to basal melting rates at the grounding line between 10.4 m

445   yr^{-1} and 28.7 m yr^{-1} for the BJR sector and between 6.2 and 13.4 m yr^{-1} for the SA sector. By comparison, a basal

446   melting rate of 22 m yr^{-1} has been observed thanks to radar measurements in the mouth of the Mercer/Whillans Ice

447 Stream located in the West Antarctic ice sheet (Marsh et al., 2016). Providing that Kt values are greater than 25 m

448 °C^{-1} yr^{-1} (or close to 50 m °C-1 yr^{-1}), the region of the BJR ice stream responds to basal melting perturbations with

449 basal melting rates similar to those observed in some parts of WAIS. However, the ice loss is restricted to the very

450 edge of the ice sheet and the BKIS retreat is negligible. This raises the question as to whether the basal melting

451 exerts a stronger influence on longer time scales. Therefore, we also investigated the ice sheet behavior after 10 000

452 model years.
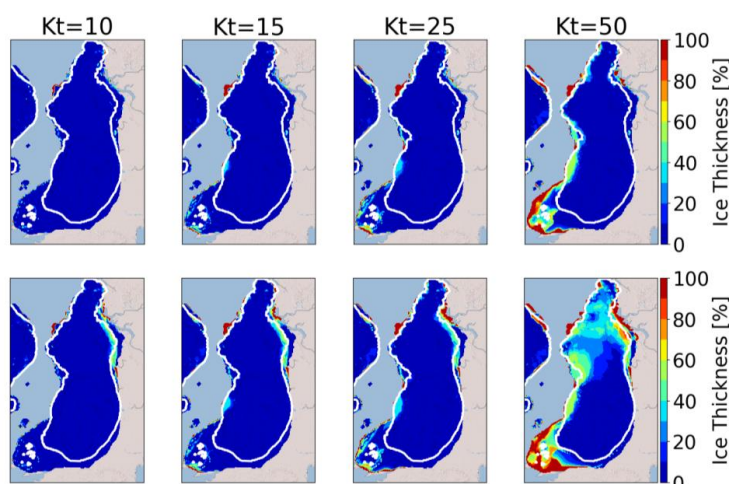
454 **Figure 8:** Multi-model mean of the ice thickness lost after 1000 (top) and 10 000 (bottom) GRISLI model years

455 in the EXP3.1 experiments with respect to the ice thickness of the LGM ice sheet. (red: 100% lost). The white line

456 corresponds to the common ice sheet mask of the five models, i.e., where the multi-model mean is computed on

457 the 5 models.

458 A similar behavior is observed after 10 000 years for Kt between 10 and 25 m °C^{-1} yr^{-1}, with the exception of the

459 southern part of BKIS bordering the Kara Sea where a 30% to 50% ice thickness decrease, with respect to the

460 initial one, is obtained. For Kt=50 m °C^{-1} yr^{-1}, more than 40% of ice loss is simulated for BKIS, and up to 60% in

461 the BJR sector. As previously mentioned, this large ice thickness decrease in the center of BKIS is highly GCM-

462 dependent, and is only observed in simulations forced by the MIROC and MPI models (Fig. SP5

463 As the basal melting parameterization is expressed as a quadratic function of the oceanic temperatures, we may

464 expect a different sensitivity of EIS when the oceanic temperatures increase (EXP3.2). Results of the EXP3.2

465 experiments are shown in figure SP7. Perturbations of oceanic temperatures between +0.5°C and +1.5°C lead to

466 basal melting rates at the grounding line of the BJR sector of less than 3.8 m yr^{-1}. This is well below the threshold

467 suggested by the results of the EXP3.1 experiments (between 10.4 and 30 m yr^{-1}), and no significant ice loss is

468 simulated after 10 000 years of simulation.

469 For larger perturbations (+7.5°C and +10°C), larger values of the basal melting rates are obtained in the BJR (11.6

470 and 17.5 m yr^{-1}), in the SA (10.8 and 15.6 m yr^{-1}) and in the MN sectors (11.5 and 17.4 m yr^{-1}) after 10 000 model

471 years. A perturbation of 7.5°C does not trigger the ice retreat because of a too low basal melting. By contrast, when

472 the perturbation reaches +10°C, a similar behavior to that simulated with Kt=50 m °C^{-1} yr^{-1} (EXP3.1) is obtained.

473 On the other hand, for simulations forced by IPSL-CM5A2 and IPSL-CM5A-LR, an increase in oceanic

474 temperatures of +10°C allows us to observe a sensitivity of BKIS in the SA sector (see Fig SP8) after 1000 years

475 of simulations, which leads to a total retreat of the eastern part of BKIS after 10000 years.

476 These results show that the BJR, MN and SA regions are sensitive to sub-shelf melting providing that the basal

477 melt exceeds a certain threshold obtained for Kt values greater than 25 m °C⁻¹ yr⁻¹ (and greater than 10 m °C⁻¹ yr⁻

478 ¹ for the MN sector) or for a rise in oceanic temperature greater than 7.5°C. From the combination of EXP3.1 and

479 EXP3.2 experiments, it appears that the threshold is between 11.6 m yr⁻¹ and 17.5 m yr⁻¹ for the BJR sector,

480 between 6.2 and 13.4 m yr⁻¹ for the SA sector and lower than 7.5 m yr⁻¹ for the MN sector. Moreover, our results

481 also suggest that the large retreat of one single ice stream has the ability to favor the total retreat of the whole of

482 BKIS

483 4.2.3 EXP4: Combined effects of basal melting and surface air temperatures

484 Results presented in the previous section suggest that sub-shelf melting has only a poor impact on the EIS

485 destabilization for Kt perturbations below a certain threshold estimated to lie between 25 and 50 m °C⁻¹ yr⁻¹, or

486 below a + 10°C increase of oceanic temperatures. However, increases in surface melting due to atmospheric

487 warming may lead to changes in the geometry of the grounded ice sheet and floating ice shelves. In turn, changes

488 in the EIS configuration may alter the EIS sensitivity to basal melting. To test this hypothesis, we combined surface

489 air temperature perturbations with basal melting perturbations (EXP4) and compared the results with those of the

490 EXP1 experiments. Figure 9 displays the difference in the total BKIS ice volume after 1000 years between EXP4

491 and EXP1 experiments (ΔV_{4_1}) for different surface atmospheric temperature perturbations ($\Delta T = +2°C, +3°C$ and

492 +4°C) and Kt values fixed to 25 and 50 m °C⁻¹ yr⁻¹ (negatives values are associated to a greater ice loss in EXP4

493 than in EXP1). For both Kt perturbations (Kt = 25 and 50 m °C⁻¹ yr⁻¹), no significant difference in the ΔV_{4_1} values

494 (computed for the different ΔT perturbations) is observed in simulations forced by IPSL-CM5A2 and IPSL-

495 CM5A-LR. This illustrates the poor sensitivity of BKIS to basal melting with the IPSL climate forcings. As

496 explained in section 4.2.2, this low sensitivity is due to the cold oceanic temperatures simulated in both IPSL

497 models (see Fig. SP6). For the three other simulations (forced by MIROC-ESM, MPI-ESM-P, and MPI-ESM1.2),

498 the ice volume difference is clearly amplified with higher ΔT levels, especially when the Kt transfer coefficient is

499 higher. For example, for Kt=50 m°C⁻¹yr⁻¹, the difference in ΔV_{4_1} values between the initial ice sheet configuration

500 ($\Delta T = 0°C$) and $\Delta T = 4°C$ is ~60 000 km³ with MPI-ESM-P, against ~20 000 km³ when Kt=50 m°C⁻¹yr⁻¹. A

501 similar behavior is observed for simulations forced by MIROC-ESM (~110 000 km³) and MPI-ESM1.2 (~60 000

502 km³). To better illustrate the impact of the combination of both temperature and basal melting perturbations, we

503 plotted the evolution of ice loss every 1kyr as simulated in the EXP1 ($\Delta T = +4°C$), EXP3 (Kt=50 m°C⁻¹yr⁻¹) and

504 EXP4 experiments in figures SP9 to SP11. For the simulation forced by MIROC-ESM (Fig. SP11), the largest part

505 of the deglaciation signal is dominated by increased atmospheric temperatures in the EXP4 (see Fig SP11).

506 Simulations forced by MPI-ESM-P and MPI-ESM1.2 have a different behaviour (Figs SP9 and SP10) and show a

507 significant difference between EXP1 and EXP4 and between EXP3 and EXP4. In the EXP3 experiment, the SA

508 sector appears to be highly sensitive, mainly due to high ocean temperatures (> 3°C, see fig SP6) in contrast to the

509 BJR sector where only a part has deglaciated after 10 000 years. However, in the EXP4 experiment, in which near-

510 surface temperature and basal melting are combined, BKIS starts to retreat after 1000 years and has almost entirely

melted after 10 000 years. This suggests that the BKIS deglaciation is initially triggered by surface warming but
is further amplified by basal melting.
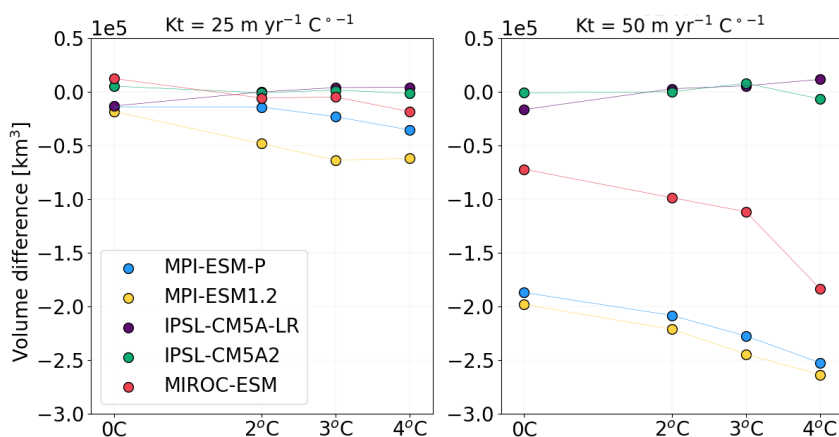
Figure 9: Differences of the ice volume lost between EXP4 and EXP1 (ΔV_{4_1}) after 1000 years for Kt=25 m °C^{-1}
yr^{-1} (left) and Kt=50 m °C^{-1} yr^{-1} (right).

4.2.5 Exp5: Sea level

In the previous simulations, the sea level forcing was fixed to -120 m (with respect to the present-day eustatic sea
level), corresponding to the estimated eustatic level at the LGM (Peltier et al., 2002). In this series of experiments,
we quantify the sensitivity of the EIS to different sea level forcings.

The multi-model mean difference between the ice thickness after 1000 GRISLI model years and the initial ice
thickness (sea level = -120 m) is displayed in Figure 10 for the different sea level elevations ranging from -115 m
to 0 m. After 1000 years of simulation, for sea levels ranging from -115 m to -105 m, no significant differences
are observed with respect to the reference simulation (i.e., - 120 m). For larger perturbations, the MNIS sector
appears to be the most sensitive. As an example, for a sea level of – 90 m, an ice loss of ~40 % is simulated in this
area, and an almost complete retreat is obtained for a sea level higher than -60m, with an ice thickness decrease of
up to 80%-100%. Although sea level elevations of -90 m and – 60 m are considerably larger than the global mean
sea level at the LGM, they are consistent with the local sea level variations that could be as high as -70 m as
suggested by Gowan et al. (2021). However, for the other sectors (BJR, SA, NCIS), ice thickness decrease is only
obtained for sea levels higher than -30 m which is largely out of the range advanced by Gowan et al. (2021). As a
result, this series of experiments suggest that the elevation of sea level has only played a marginal role at the
beginning of the EIS deglaciation.
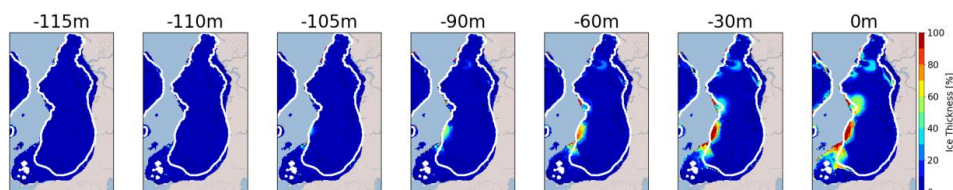
Figure 10: Multi-model mean of the ice thickness lost after 1000 model years in the EXP5 with respect to the ice thickness of the LGM ice sheet. (red: 100% lost). The white line corresponds to the common ice sheet mask of the five models, i.e., where the multi-model mean is computed on the 5 models.

5. Discussion

The results of our experiments suggest that the EIS ice sheet is very sensitive to the atmospheric warming that may have occurred at the beginning of the last deglaciation. By contrast, basal melting does not seem to be a key process for triggering the retreat of the ice sheet. However, once the retreat has been initiated by the atmospheric warming, basal melting has the capability of accelerating the retreat, as supported by the results of EXP4, providing that the amount of basal melting is high enough. Nevertheless, these conclusions are strongly dependent on the ice-shelf configurations. Indeed, unconfined ice shelves do not exert an efficient buttressing effect (i.e. the stress that the ice shelves exert at the grounding line) and their removal has almost no impact on the dynamics of the grounded ice sheet (Gundmundsson et al., 2013, Fürst et al., 2016). By contrast, thinning of confined ice shelves through basal melting produce a weakening of the buttressing effect, implying an acceleration of the grounded ice streams and ultimately a substantial ice discharge in the ocean. This sequence of events was observed in the Antarctic Peninsula after the collapse of the Larsen B Ice Shelf in 2002 (Rignot et al., 2004; De Rydt et al., 2015). Moreover, using a high-resolution ice sheet model (500 mx500 m near the grounding line), Gandy et al. (2018) showed the significant impact of the melting of confined ice shelves on the destabilization of ice streams in Northwest Scotland during the last deglaciation. In our study, the extent of the confined ice shelves in the simulated EIS at the end of the spin-up experiments is very small (Fig. 3). This likely explains why the EIS appears poorly sensitive to basal melting and why strong perturbations of the Kt coefficient or oceanic temperatures are required to simulate ice-shelf thinning in the regions of the main ice streams.

The small sensitivity to the oceanic forcing simulated in the EXP3 experiments contradicts the conclusions of previous modeling studies of the EIS behavior during the last glacial period (Alvarez-Solas et al., 2019) and the last deglaciation (Petrini et al., 2020). Both conclude that oceanic temperatures are the main driver of the EIS destabilization. Their findings are all the more surprising as they both use an ice-sheet model (GRISLI1.0) similar to ours (GRISLI2.0). However, several differences can be noticed between their modeling approach and that of the present study. First, GRISLI1.0 does not include a parameterization of the ice flux at the grounding line. Therefore, it should be easier with our model to trigger the EIS retreat through basal melting because GRISLI2.0 includes key processes to simulate the marine ice sheet instability. To verify this issue, we performed additional simulations similar to the EXP3 ones by removing the grounding line flux parameterization, and as expected, results clearly show that the removal of this parameterization limits the ice loss (not shown). One of the most likely explanation of the disagreement between our findings and those of previous studies (Alvarez-Solas et al., 2019; Petrini et al., 2020) relies on the procedure followed in the spin-up experiments. Both built their initial state in the

567 same way. To favor the EIS build-up, they fixed the basal melting to 0.1 m yr⁻¹ during their ice sheet spin-up.

568 Starting from the EIS configuration obtained at the end of the sin-up experiment, they used a linear (Alvarez-Solas

569 et al., 2019) or quadratic (Petrini et al., 2020) basal melting parameterization depending on oceanic temperature to

570 simulate the last glacial period (Alvarez-Solas et al., 2019) or the last deglaciation (Petrini et al., 2020) of EIS. In

571 doing so, there is a methodological inconsistency between the spin-up simulation and the subsequent experiments.

572 To investigate the effect of such inconsistency on the EIS deglaciation, we followed their spin-up methodology

573 (homogeneous basal melting) instead of the one described in Section 2.3. The resulting LGM ice sheets resemble

574 those presented in Sec. 3.1, except that the MIROC-ESM forcing produces large ice shelves in the Greenland and

575 Norwegian seas. We then applied the same perturbations as in EXP3 on these alternative ice sheets with a basal

576 melting parameterization depending on the oceanic temperature and salinity (see Eq7). We display in figure 11 the

577 percentage of ice thickness lost after 10000 years with respect to the initial configuration for Kt ranging from 15

578 to 50 m °C⁻¹ yr⁻¹ for this new series of experiments. Compared to EXP3, we show that the EIS now presents a

579 much more significant sensitivity in the BIIS and FIS for a perturbation of Kt=50 m °C⁻¹ yr⁻¹. These results illustrate

580 the extent to which the conclusions drawn for the driving mechanisms of the EIS destabilization are strongly

581 dependent on the initial state. However, we argue that the approach followed in the present paper is more consistent

582 as the basal melting parameterization is exactly the same for the spin-up procedure and the sensitivity experiments.

583 Finally, another difference that deserves to be mentioned is that Petrini et al, (2020) used a climate index (based

584 on the transient simulation of Liu et al., (2009). This method ensures that both the atmospheric and oceanic

585 temperatures increase concomitantly to their pre-industrial levels. As a result, we cannot exclude that the key role

586 of basal melting in their simulated deglaciation is not amplified by the effect of atmospheric warming, similarly to

587 the conclusions drawn from our EXP4 results.
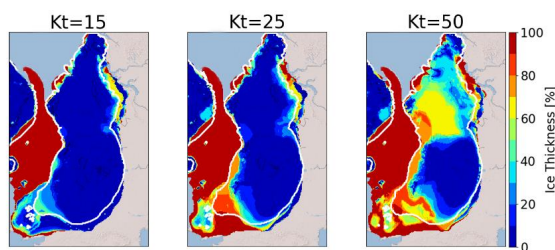
588

589 **Figure 11:** Multi-model mean of the ice thickness loss compared to the initial ice sheet for different basal melting

590 perturbations. LGM ice sheets are built by fixing the basal melting to 0.1 m yr⁻¹ (as in Petrini et al., 2020; Alvarez-

591 Solas et al., 2019). Note that the significant decrease in ice thickness in the Norwegian and Greenland seas is due

592 to the simulation of ice shelves in the new spin-up for the MIROC-ESM forcing (see Fig. SP12). These ice shelves

593 are extremely sensitive to a change in the basal melt. The white line indicates the areas where the multi-model

594 mean is done on the 5 models.

595 **6. Conclusion**

596 In this paper, we used off-line GRISLI2.0 simulations forced by PMIP3/PMIP4 models to investigate the key

597 mechanisms driving the retreat of the Eurasian ice complex at the beginning of the last deglaciation. We gave a

598 special attention to the understanding of the processes responsible for the destabilization of the marine-based parts

599 of the Eurasian ice sheets as GRISLI2.0 includes and explicit calculation of the ice flux at the grounding line which

600 is expected to account for the representation of the marine ice sheet instability. We first showed that, due to too

601 strong climate biases in some GCMs at the LGM, only 5 out of 10 GCMs succeeded in building an ice sheet in

602 agreement with the reconstructions.

603 The sensitivity experiments have been designed to test the response of the simulated Eurasian ice sheets to surface

604 climate, oceanic temperature and sea level perturbations. Our results highlight the high EIS sensitivity to a change

605 in surface atmospheric temperatures. While basal melting does not seem to be the main driver of the ice sheet

606 retreat, we showed that its effect is clearly amplified by the atmospheric warming.

607 These results contradict those of previous studies mentioning the central role of the ocean on the deglaciation of

608 BKIS. However, we argue that parts of this disagreement are related to the way the climatic forcing is done

609 (absolute climatic fields, anomalies or climatic indexes) and the procedure followed for building the initial state

610 of EIS and to the presence of confined or unconfined ice shelves at the LGM.

611 This study highlights several differences regarding the respective behaviors of the Eurasian ice sheet during the

612 last deglaciation and the present-day West Antarctic ice sheet. While EIS appears primarily sensitive to the

613 atmospheric forcing, WAIS is mainly driven by dynamic ice discharges triggered by the ocean warming. In

614 addition, WAIS is characterized by large areas of confined ice shelves exerting a buttressing effect on the grounded

615 ice whereas most of the ice shelves in our simulated LGM EIS are unconfined. However, as temperatures rise in

616 the future, larger amounts of meltwater will be produced on the surface of the ice shelves (Kittel et al., 2021),

617 favouring potentially the ice-shelf disintegration through hydrofracturing (Banwell et al., 2013; Lai et al., 2020).

618 Although, this process differs from basal melting, it could bring WAIS into a similar configuration to the past

619 Eurasian ice sheet.

620 **Data availability.** The source data of the experiments presented in the main text of the paper are available on the

621 Zenodo repository with the digital object identifier https://doi.org/10.5281/zenodo.7528183 (van Aalderen et al,

622 2023).

623 **Author contributions.** All authors designed the study. VVA performed the numerical experiments. All authors

624 contributed to the analysis of model results. VVA and SC wrote the manuscript with inputs from CD and AQ.

625 **Competing interests.** The authors declare that they have no conflict of interest

626 **Acknowledgements.** Victor van Aalderen is funded by the French National Research Agency (Grant: ANR-19-

627 CE01-15). We acknowledge the World Climate Research Programme's Working Group on Coupled Modelling,

628 which is responsible for the Paleoclimate Modelling Intercomparison Project (PMIP) and we thank the climate

629 modeling groups (listed in Table 1 of this paper) for producing and making available their model output. This work

630 benefited from productive exchanges with N. Jourdain and D. Swingedouw.

631

632

633

634

635 **References**

636 Abe-Ouchi, A., Saito, F., Kageyama, M., Braconnot, P., Harrison, S. P., Lambeck, K., Otto-Bliesner, B. L., Peltier,
637   W. R., Tarasov, L., Peterschmitt, J. Y., & Takahashi, K., Ice-sheet configuration in the CMIP5/PMIP3 Last
638   Glacial Maximum experiments., *Geoscientific Model Development*, *8*(11), 3621–3637,
639   https://doi.org/10.5194/gmd-8-3621-2015, 2015

640 Adloff, M., Reick, C. H., & Claussen, M., Earth system model simulations show different feedback strengths of
641   the terrestrial carbon cycle under glacial and interglacial conditions. *Earth System Dynamics*, *9*(2), 413–425,
642   https://doi.org/10.5194/esd-9-413-2018, 2018

643 Alvarez-Solas, J., Banderas, R., Robinson, A., & Montoya, M., Ocean-driven millennial-scale variability of the
644   Eurasian ice sheet during the last glacial period simulated with a hybrid ice-sheet–shelf model. *Climate of the*
645   *Past*, *15*(3), 957–979, https://doi.org/10.5194/cp-15-957-2019, 2019

646 Amante, C. and Eakins, B W. ETOPO1 arc-minute global relief model: procedures, data sources and analysis. Vol.
647   NESDIS NGDC-24. National Geophysical Data Center, Boulder, CO, USA,
648   https://repository.library.noaa.gov/view/noaa/1163, 2009

649 Andreassen, K., & Winsborrow, M., Signature of ice streaming in Bjørnøyrenna, Polar North Atlantic, through the
650   Pleistocene and implications for ice-stream dynamics. *Annals of Glaciology*, *50*(52), 17–26,
651   https://doi.org/10.3189/172756409789624238, 2009

652 Annan, J. D., Hargreaves, J. C., Mauritsen, T. A new global surface temperature reconstruction for the Last Glacial
653   Maximum., Climate of the Past, 18(8), 1883-1896, https://doi.org/10.5194/cp-18-1883-2022, 2022

654 Banwell, Alison F., Douglas R. MacAyeal, and Olga V. Sergienko. Breakup of the Larsen B Ice Shelf triggered
655   by chain reaction drainage of supraglacial lakes. Geophysical Research Letters 40.22, 5872-5876,
656   https://doi.org/10.1002/2013GL057694, 2013.

657 Beckmann, A., & Goosse, H., A parameterization of ice shelf–ocean interaction for climate models. *Ocean*
658   *Modelling*, *5*(2), 157–170, https://doi.org/10.1016/s1463-5003(02)00019-7, 2003

659 Beghin, P., Charbit, S., Dumas, C., Kageyama, M., Roche, D. M., & Ritz, C. Interdependence of the growth of the
660   Northern Hemisphere ice sheets during the last glaciation: the role of atmospheric circulation. *Climate of the*
661   *Past*, *10*(1), 345–358, https://doi.org/10.5194/cp-10-345-2014, 2014

662 Briggs, R. D., Pollard, D., & Tarasov, L., A data-constrained large ensemble analysis of Antarctic evolution since
663   the Eemian. Quaternary Science Reviews, 103, 91-115, https://doi.org/10.1016/j.quascirev.2014.09.003, 2014

664   Colleoni, F., Masina, S., Cherchi, A., Navarra, A., Ritz, C., Peyaud, V., & Otto-Bliesner, B. Modeling Northern
665   Hemisphere ice-sheet distribution during MIS 5 and MIS 7 glacial inceptions. *Climate of the Past*, *10*(1), 269–
666   291, https://doi.org/10.5194/cp-10-269-2014, 2014

667   De Rydt, J., Gudmundsson, G. H., Rott, H., & Bamber, J. L. Modeling the instantaneous response of glaciers after
668   the collapse of the Larsen B Ice Shelf. Geophysical Research Letters, 42(13), 5355-5363,
669   https://doi.org/10.1002/2015GL064355, 2015

670   Dowdeswell, J. A., Canals, M., Jakobsson, M., Todd, B. J., Dowdeswell, E. K., & Hogan, K. A. The variety and
671   distribution of submarine glacial landforms and implications for ice-sheet reconstruction. *Geological Society,*
672   *London, Memoirs*, *46*(1), 519–552, https://doi.org/10.1144/m46.183, 2016

673   Dowdeswell, J. A., Montelli, A., Akhmanov, G., Solovyeva, M., Terekhina, Y., Mironyuk, S., & Tokarev, M. Late
674   Weichselian ice-sheet flow directions in the Russian northern Barents Sea from high-resolution imagery of
675   submarine glacial landforms. *Geology*, *49*(12), 1484–1488, https://doi.org/10.1130/g49252.1, 2021

676   Dufresne, J. L., Foujols, M. A., Denvil, S., Caubel, A., Marti, O., Aumont, O., Balkanski, Y., Bekki, S., Bellenger,
677   H., Benshila, R., Bony, S., Bopp, L., Braconnot, P., Brockmann, P., Cadule, P., Cheruy, F., Codron, F., Cozic,
678   A., Cugnet, D., Vuichard, N., Climate change projections using the IPSL-CM5 Earth System Model: from
679   CMIP3 to CMIP5. *Climate Dynamics*, *40*(9–10), 2123–2165, https://doi.org/10.1007/s00382-012-1636-1,
680   2013

681   Durand, G., Gagliardini, O., de Fleurian, B., Zwinger, T., & le Meur, E. Marine ice sheet dynamics: Hysteresis
682   and neutral equilibrium. *Journal of Geophysical Research*, *114*(F3), https://doi.org/10.1029/2008jf001170,
683   2009

684   Fürst, J. J., Durand, G., Gillet-Chaulet, F., Tavard, L., Rankl, M., Braun, M., & Gagliardini, O. The safety band of
685   Antarctic ice shelves. Nature Climate Change, 6(5), 479-482, https://doi.org/10.1038/nclimate2912, 2016.

686   Gandy, N., Gregoire, L. J., Ely, J. C., Clark, C. D., Hodgson, D. M., Lee, V., Bradwell, T., & Ivanovic, R. F.
687   Marine ice sheet instability and ice shelf buttressing of the Minch Ice Stream, northwest Scotland. *The*
688   *Cryosphere*, *12*(11), 3635–3651, https://doi.org/10.5194/tc-12-3635-2018, 2018

689   Gandy, N., Gregoire, L. J., Ely, J. C., Cornford, S. L., Clark, C. D., & Hodgson, D. M. Collapse of the Last Eurasian
690   Ice Sheet in the North Sea Modulated by Combined Processes of Ice Flow, Surface Melt, and Marine Ice Sheet
691   Instabilities. *Journal of Geophysical Research: Earth Surface*, *126*(4), https://doi.org/10.1029/2020jf005755,
692   2021

693   Goelzer, H., Nowicki, S., Payne, A., Larour, E., Seroussi, H., Lipscomb, W. H., Gregory, J., Abe-Ouchi, A.,
694   Shepherd, A., Simon, E., Agosta, C., Alexander, P., Aschwanden, A., Barthel, A., Calov, R., Chambers, C.,
695   Choi, Y., Cuzzone, J., Dumas, C.,et al,. The future sea-level contribution of the Greenland ice sheet: a multi-

696 model ensemble study of ISMIP6. *The Cryosphere*, *14*(9), 3071–3096, https://doi.org/10.5194/tc-14-3071-
697 2020, 2020

698 Gowan, E. J., Zhang, X., Khosravi, S., Rovere, A., Stocchi, P., Hughes, A. L. C., Gyllencreutz, R., Mangerud, J.,
699 Svendsen, J. I., & Lohmann, G. A new global ice sheet reconstruction for the past 80 000 years. *Nature*
700 *Communications*, *12*(1), https://doi.org/10.1038/s41467-021-21469-w, 2021

701 Gudlaugsson, E., Humbert, A., Andreassen, K., Clason, C. C., Kleiner, T., & Beyer, S. Eurasian ice-sheet dynamics
702 and   sensitivity   to   subglacial   hydrology.   *Journal   of   Glaciology*,   *63*(239),   556–564,
703 https://doi.org/10.1017/jog.2017.21, 2017.

704 Gundmundsson, G.H. : Ice-shelf buttressing and the stability of marine ice sheets, The Cryosphere, 7, 647-655,
705 doi: 10.5194/tc-7-647-2013, 2013.

706 Hajima, T., Watanabe, M., Yamamoto, A., Tatebe, H., Noguchi, M. A., Abe, M., Ohgaito, R., Ito, A., Yamazaki,
707 D., Okajima, H., Ito, A., Takata, K., Ogochi, K., Watanabe, S., & Kawamiya, M. Development of the MIROC-
708 ES2L Earth system model and the evaluation of biogeochemical processes and feedbacks. *Geoscientific Model*
709 *Development*, *13*(5), 2197–2244, https://doi.org/10.5194/gmd-13-2197-2020, 2020

710 Holland, P. R., Jenkins, A., & Holland, D. M. The Response of Ice Shelf Basal Melting to Variations in Ocean
711 Temperature. *Journal of Climate*, *21*(11), 2558–2572, https://doi.org/10.1175/2007jcli1909.1, 2008

712 Hughes, A. L. C., Gyllencreutz, R., Lohne, Y. S., Mangerud, J., & Svendsen, J. I. The last Eurasian ice sheets – a
713 chronological   database   and   time-slice   reconstruction,   DATED-1.   *Boreas*,   *45*(1),   1–45,
714 https://doi.org/10.1111/bor.12142, 2016

715 Hutter, K. The Response of a Glacier or an Ice Sheet to Seasonal and Climatic Changes. *Theoretical Glaciology*,
716 333–423, https://doi.org/10.1007/978-94-015-1167-4_6, 1983

717 Kageyama, M., Harrison, S. P., Kapsch, M. L., Lofverstrom, M., Lora, J. M., Mikolajewicz, U., Sherriff-Tadano,
718 S., Vadsaria, T., Abe-Ouchi, A., Bouttes, N., Chandan, D., Gregoire, L. J., Ivanovic, R. F., Izumi, K.,
719 LeGrande, A. N., Lhardy, F., Lohmann, G., Morozova, P. A., Ohgaito, R., . . . Zhu, J. The PMIP4 Last Glacial
720 Maximum experiments: preliminary results and comparison with the PMIP3 simulations. *Climate of the Past*,
721 *17*(3), 1065–1089, https://doi.org/10.5194/cp-17-1065-2021, 2021

722 Kittel, C., Amory, C., Agosta, C., Jourdain, N. C., Hofer, S., Delhasse, A., Doutreloup, S., Huot, P.-V., Lang, C.,
723 Fichefet, T., and Fettweis, X.: Diverging future surface mass balance between the Antarctic ice shelves and
724 grounded ice sheet, The Cryosphere, 15, 1215–1236, https://doi.org/10.5194/tc-15-1215-2021, 2021

725 Konrad, H., Shepherd, A., Gilbert, L., Hogg, A. E., McMillan, M., Muir, A., & Slater, T. Net retreat of Antarctic
726 glacier grounding lines. Nature Geoscience, 11(4), 258-262, https://doi.org/10.1038/s41561-018-0082-z, 2018

727 Ladant, J. B., Donnadieu, Y., Lefebvre, V., & Dumas, C. The respective role of atmospheric carbon dioxide and
728 orbital parameters on ice sheet evolution at the Eocene-Oligocene transition. *Paleoceanography*, *29*(8), 810–
729 823, https://doi.org/10.1002/2013pa002593, 2014

730 Lai, CY., Kingslake, J., Wearing, M.G. et al. Vulnerability of Antarctica's ice shelves to meltwater-driven fracture.
731 Nature 584, 574–578, https://doi.org/10.1038/s41586-020-2627-8, 2020

732 Lambeck, K. Late Devensian and Holocene shorelines of the British Isles and North Sea from models of glacio-
733 hydro-isostatic   rebound.   *Journal   of   the   Geological   Society*,   *152*(3),   437–448,
734 https://doi.org/10.1144/gsjgs.152.3.0437, 1995

735 Lambeck, K. Glaciation and sea-level change for Ireland and the Irish Sea since Late Devensian/Midlandian time.
736 *Journal of the Geological Society*, *153*(6), 853–872, https://doi.org/10.1144/gsjgs.153.6.0853, 1996

737 Lambeck, K., Purcell, A., Zhao, J., & Svensson, N. O. The Scandinavian Ice Sheet: from MIS 4 to the end of the
738 Last Glacial Maximum. *Boreas*, *39*(2), 410–435, https://doi.org/10.1111/j.1502-3885.2010.00140.x, 2010

739 Lambeck, K., Rouby, H., Purcell, A., Sun, Y., & Sambridge, M. Sea level and global ice volumes from the Last
740 Glacial Maximum to the Holocene. Proceedings of the National Academy of Sciences, 111(43), 15296-15303,
741 https://doi.org/10.1073/pnas.1411762111, 2014

742 Le Clec'h, S., Quiquet, A., Charbit, S., Dumas, C., Kageyama, M., & Ritz, C. A rapidly converging initialisation
743 method to simulate the present-day Greenland ice sheet using the GRISLI ice sheet model (version 1.3).
744 *Geoscientific Model Development*, *12*(6), 2481–2499, https://doi.org/10.5194/gmd-12-2481-2019, 2019

745 Liu, Z., Otto-Bliesner, B. L., He, F., Brady, E. C., Tomas, R., Clark, P. U., ... & Cheng, J. Transient simulation of
746 last deglaciation with a new mechanism for Bølling-Allerød warming. science, 325(5938), 310-314,
747 https://doi.org/10.1126/science.1171041, 2009.

748 MacAyeal, D. R. Large-scale ice flow over a viscous basal sediment: Theory and application to ice stream B,
749 Antarctica.   *Journal   of   Geophysical   Research: Solid   Earth*,   *94*(B4),   4071–4087,
750 https://doi.org/10.1029/jb094ib04p04071, 1989

751 MARGO Project Members, Constraints on the magnitude and patterns of ocean cooling at the Last Glacial
752 Maximum. Nature Geoscience, vol. 2, no 2, p. 127-132, https://doi.org/10.1038/ngeo411 ,2009.

753 Marsh, O. J., Fricker, H. A., Siegfried, M. R., Christianson, K., Nicholls, K. W., Corr, H. F., & Catania, G. High
754 basal melting forming a channel at the grounding line of Ross Ice Shelf, Antarctica. Geophysical Research
755 Letters, 43(1), 250-255, https://doi.org/10.1002/2015GL066612, 2016.

756 Mauritsen, T., Bader, J., Becker, T., Behrens, J., Bittner, M., Brokopf, R., Brovkin, V., Claussen, M., Crueger, T.,
757 Esch, M., Fast, I., Fiedler, S., Fläschner, D., Gayler, V., Giorgetta, M., Goll, D. S., Haak, H., Hagemann, S.,

758   Hedemann, C., Roeckner, E. Developments in the MPI-M Earth System Model version 1.2 (MPI-ESM1.2) and
759   Its Response to Increasing CO 2. *Journal of Advances in Modeling Earth Systems*, *11*(4), 998–1038,
760   https://doi.org/10.1029/2018ms001400, 2019

761   Mercer, J. H. Antarctic Ice and Interglacial High Sea Levels. *Science*, *168*(3939), 1605–1606,
762   https://doi.org/10.1126/science.168.3939.1605.b, 1970

763   Mouginot, J., Rignot, E., & Scheuchl, B. Continent-Wide, Interferometric SAR Phase, Mapping of Antarctic Ice
764   Velocity. *Geophysical Research Letters*, *46*(16), 9710–9718, https://doi.org/10.1029/2019gl083826, 2019

765   Nowicki, S., Goelzer, H., Seroussi, H., Payne, A. J., Lipscomb, W. H., Abe-Ouchi, A., Agosta, C., Alexander, P.,
766   Asay-Davis, X. S., Barthel, A., Bracegirdle, T. J., Cullather, R., Felikson, D., Fettweis, X., Gregory, J. M.,
767   Hattermann, T., Jourdain, N. C., Kuipers Munneke, P., Larour, E., van de Wal, R. Experimental protocol for
768   sea level projections from ISMIP6 stand-alone ice sheet models. *The Cryosphere*, *14*(7), 2331–2368,
769   https://doi.org/10.5194/tc-14-2331-2020, 2020

770   Patton, H., Hubbard, A., Andreassen, K., Auriac, A., Whitehouse, P. L., Stroeven, A. P., Shackleton, C.,
771   Winsborrow, M., Heyman, J., & Hall, A. M. Deglaciation of the Eurasian ice sheet complex. *Quaternary*
772   *Science Reviews*, *169*, 148–172, https://doi.org/10.1016/j.quascirev.2017.05.019, 2017

773   Pattyn, F. The paradigm shift in Antarctic ice sheet modelling. Nature communications, 9(1), 1-3,
774   https://doi.org/10.1038/s41467-018-05003-z, 2018.

775   Peltier, W. R. On eustatic sea level history: Last Glacial Maximum to Holocene. Quaternary Science Reviews,
776   21(1-3), 377-396, https://doi.org/10.1016/S0277-3791(01)00084-1, 2002.

777   Peltier, W. R., Argus, D. F., & Drummond, R. Space geodesy constrains ice age terminal deglaciation: The global
778   ICE-6G_C (VM5a) model. *Journal of Geophysical Research: Solid Earth*, *120*(1), 450–487,
779   https://doi.org/10.1002/2014jb011176, 2015

780   Petrini, M., Colleoni, F., Kirchner, N., Hughes, A. L., Camerlenghi, A., Rebesco, M., Lucchi, R. G., Forte, E.,
781   Colucci, R. R., Noormets, R., & Mangerud, J. Simulated last deglaciation of the Barents Sea Ice Sheet primarily
782   driven by oceanic conditions. *Quaternary Science Reviews*, *238*, 106314,
783   https://doi.org/10.1016/j.quascirev.2020.106314, 2020

784   Peyaud, V., Ritz, C., & Krinner, G. Modelling the Early Weichselian Eurasian Ice Sheets: role of ice shelves and
785   influence of ice-dammed lakes. *Climate of the Past*, *3*(3), 375–386, https://doi.org/10.5194/cp-3-375-2007,
786   2007

787   Pollard, D., & DeConto, R. M. Modelling West Antarctic ice sheet growth and collapse through the past five
788   million years. Nature, 458(7236), 329-332, https://doi.org/10.1038/nature07809, 2009

789 Pollard, D., & DeConto, R. M. Description of a hybrid ice sheet-shelf model, and application to Antarctica.
790   *Geoscientific Model Development*, *5*(5), 1273–1295, https://doi.org/10.5194/gmd-5-1273-2012, 2012

791 Polyak, L., Forman, S. L., Herlihy, F. A., Ivanov, G., & Krinitsky, P. Late Weichselian deglacial history of the
792   Svyataya (Saint) Anna Trough, northern Kara Sea, Arctic Russia. *Marine Geology*, *143*(1–4), 169–188,
793   https://doi.org/10.1016/s0025-3227(97)00096-0, 1997

794 Pritchard, H. D., Arthern, R. J., Vaughan, D. G., & Edwards, L. A. Extensive dynamic thinning on the margins of
795   the Greenland and Antarctic ice sheets. *Nature*, *461*(7266), 971–975, https://doi.org/10.1038/nature08471,
796   2009

797 Pritchard, H., Ligtenberg, S. R., Fricker, H. A., Vaughan, D. G., van den Broeke, M. R., & Padman, L. Antarctic
798   ice-sheet loss driven by basal melting of ice shelves. Nature, 484(7395), 502-505,
799   https://doi.org/10.1038/nature10968, 2012.

800 Quiquet, A., Dumas, C., Ritz, C., Peyaud, V., & Roche, D. M. The GRISLI ice sheet model (version 2.0):
801   calibration and validation for multi-millennial changes of the Antarctic ice sheet. *Geoscientific Model
802   Development*, *11*(12), 5003–5025, https://doi.org/10.5194/gmd-11-5003-2018, 2018

803 Quiquet, A., Ritz, C., Punge, H. J., & Salas Y Mélia, D. Greenland ice sheet contribution to sea level rise during
804   the last interglacial period: a modelling study driven and constrained by ice core data. *Climate of the Past*, *9*(1),
805   353–366, https://doi.org/10.5194/cp-9-353-2013, 2013

806 Quiquet, A., & Dumas, C. The GRISLI-LSCE contribution to the Ice Sheet Model Intercomparison Project for
807   phase 6 of the Coupled Model Intercomparison Project (ISMIP6)–Part 1: Projections of the Greenland ice sheet
808   evolution by the end of the 21st century. The Cryosphere, 15(2), 1015-1030, https://doi.org/10.5194/tc-15-
809   1015-2021, 2021a.

810 Quiquet, A., & Dumas, C. The GRISLI-LSCE contribution to the Ice Sheet Model Intercomparison Project for
811   phase 6 of the Coupled Model Intercomparison Project (ISMIP6)–Part 2: Projections of the Antarctic ice sheet
812   evolution by the end of the 21st century. The Cryosphere, 15(2), 1031-1052, https://doi.org/10.5194/tc-15-
813   1031-2021, 2021b.

814 Quiquet, A., Roche, D. M., Dumas, C., Bouttes, N., & Lhardy, F. Climate and ice sheet evolutions from the last
815   glacial maximum to the pre-industrial period with an ice-sheet–climate coupled model. *Climate of the Past*,
816   *17*(5), 2179–2199, https://doi.org/10.5194/cp-17-2179-2021, 2021c

817 Rasmussen, T. L., & Thomsen, E. Climate and ocean forcing of ice-sheet dynamics along the Svalbard-Barents
818   Sea ice sheet during the deglaciation ~20,000–10,000 years BP. *Quaternary Science Advances*, *3*, 100019,
819   https://doi.org/10.1016/j.qsa.2020.100019, 2021

820   Rignot, E., Casassa, G., Gogineni, P., Krabill, W., Rivera, A. U., & Thomas, R. Accelerated ice discharge from
821   the Antarctic Peninsula following the collapse of Larsen B ice shelf. Geophysical research letters, 31(18),
822   https://doi.org/10.1029/2004GL020697, 2004.

823   Rignot, E., Mouginot, J., Scheuchl, B., Van Den Broeke, M., Van Wessem, M. J., & Morlighem, M. Four decades
824   of Antarctic Ice Sheet mass balance from 1979–2017. Proceedings of the National Academy of Sciences,
825   116(4), 1095-1103, https://doi.org/10.1073/pnas.1812883116, 2019.

826   Ritz, C., Rommelaere, V., & Dumas, C. Modeling the evolution of Antarctic ice sheet over the last 420,000 years:
827   Implications for altitude changes in the Vostok region. *Journal of Geophysical Research: Atmospheres*,
828   *106*(D23), 31943–31964, https://doi.org/10.1029/2001jd900232, 2001

829   Schoof, C. Marine ice sheet stability. *Journal of Fluid Mechanics*, *698*, 62–72,
830   https://doi.org/10.1017/jfm.2012.43, 2012

831   Sejrup, H. P., Haflidason, H., Aarseth, I., King, E., Forsberg, C. F., Long, D., & Rokoengen, K. Late Weichselian
832   glaciation history of the northern North Sea. *Boreas*, *23*(1), 1–13, https://doi.org/10.1111/j.1502-
833   3885.1994.tb00581.x, 1994

834   Sejrup, H. P., Hjelstuen, B. O., Patton, H., Esteves, M., Winsborrow, M., Rasmussen, T. L., ... & Hubbard, A. The
835   role of ocean and atmospheric dynamics in the marine-based collapse of the last Eurasian Ice Sheet.
836   Communications Earth & Environment, 3(1), 1-10, https://doi.org/10.1038/s43247-022-00447-0, 2022.

837   Sepulchre, P., Caubel, A., Ladant, J. B., Bopp, L., Boucher, O., Braconnot, P., Brockmann, P., Cozic, A.,
838   Donnadieu, Y., Dufresne, J. L., Estella-Perez, V., Ethé, C., Fluteau, F., Foujols, M. A., Gastineau, G., Ghattas,
839   J., Hauglustaine, D., Hourdin, F., Kageyama, M., et al. IPSL-CM5A2 – an Earth system model designed for
840   multi-millennial climate simulations. *Geoscientific Model Development*, *13*(7), 3011–3053,
841   https://doi.org/10.5194/gmd-13-3011-2020, 2020

842   Seroussi, H., Nowicki, S., Payne, A. J., Goelzer, H., Lipscomb, W. H., Abe-Ouchi, A., Agosta, C., Albrecht, T.,
843   Asay-Davis, X., Barthel, A., Calov, R., Cullather, R., Dumas, C., Galton-Fenzi, B. K., Gladstone, R., Golledge,
844   N. R., Gregory, J. M., Greve, R., Hattermann, T. et al. ISMIP6 Antarctica: a multi-model ensemble of the
845   Antarctic ice sheet evolution over the 21st century. *The Cryosphere*, *14*(9), 3033–3070,
846   https://doi.org/10.5194/tc-14-3033-2020, 2020

847   Shapiro, N., Ritzwoller, M. Inferring surface heat flux distributions guided by a global seismic model: particular
848   application to Antarctica. *Earth and Planetary Science Letters*, *223*(1–2), 213–224,
849   https://doi.org/10.1016/j.epsl.2004.04.011, 2004

850   Solgaard, A., Kusk, A., Merryman Boncori, J. P., Dall, J., Mankoff, K. D., Ahlstrøm, A. P., ... & Fausto, R. S.
851   Greenland ice velocity maps from the PROMICE project. Earth System Science Data, 13(7), 3491-3512,
852   https://doi.org/10.5194/essd-13-3491-2021, 2021.

853   Stokes, C. R., & Clark, C. D. Palaeo-ice streams. Quaternary Science Reviews, 20(13), 1437-1457,
854   https://doi.org/10.1016/S0277-3791(01)00003-8, 2001.

855   Sueyoshi, T., Ohgaito, R., Yamamoto, A., Chikamoto, M. O., Hajima, T., Okajima, H., Yoshimori, M., Abe, M.,
856   O'ishi, R., Saito, F., Watanabe, S., Kawamiya, M., & Abe-Ouchi, A. Set-up of the PMIP3 paleoclimate
857   experiments conducted using an Earth system model, MIROC-ESM. *Geoscientific Model Development*, *6*(3),
858   819–836, https://doi.org/10.5194/gmd-6-819-2013, 2013

859   Svendsen, J. Late Quaternary ice sheet history of northern Eurasia. *Quaternary Science Reviews*, *23*(11–13), 1229–
860   1271, https://doi.org/10.1016/j.quascirev.2003.12.008, 2004

861   Svendsen, J. I., Briner, J. P., Mangerud, J., & Young, N. E. Early break-up of the Norwegian Channel Ice Stream
862   during   the   Last   Glacial   Maximum.   *Quaternary   Science   Reviews*,   *107*,   231–242,
863   https://doi.org/10.1016/j.quascirev.2014.11.001, 2015

864   Szuman, I., Kalita, J. Z., Ewertowski, M. W., Clark, C. D., & Livingstone, S. J. Dynamics of the last Scandinavian
865   Ice Sheet's southernmost sector revealed by the pattern of ice streams. *Boreas*, *50*(3), 764–780,
866   https://doi.org/10.1111/bor.12512, 2021

867   Tarasov, L., & Richard Peltier, W. Greenland glacial history and local geodynamic consequences. *Geophysical
868   Journal International*, *150*(1), 198–229, https://doi.org/10.1046/j.1365-246x.2002.01702.x, 2002

869   Tarasov, L, Dyke, A. S., Neal, R. M., & Peltier, W. R. A data-calibrated distribution of deglacial chronologies for
870   the North American ice complex from glaciological modeling. Earth and Planetary Science Letters, 315, 30-
871   40, https://doi.org/10.1016/j.epsl.2011.09.010, 2012.

872   Tierney, J.E., Zhu, J., King, J. et al. Glacial cooling and climate sensitivity revisited. Nature 584, 569–573, 2020,
873   https://doi.org/10.1038/s41586-020-2617-x

874   Tsai, V. C., & Gudmundsson, G. H. An improved model for tidally modulated grounding-line migration. *Journal
875   of Glaciology*, *61*(226), 216–222, https://doi.org/10.3189/2015jog14j152, 2015

876   Ullman, D. J., LeGrande, A. N., Carlson, A. E., Anslow, F. S., & Licciardi, J. M. Assessing the impact of
877   Laurentide Ice Sheet topography on glacial climate. *Climate of the Past*, *10*(2), 487–507.
878   https://doi.org/10.5194/cp-10-487-2014, 2014

879   Voldoire, A., Sanchez-Gomez, E., Salas Y Mélia, D., Decharme, B., Cassou, C., Sénési, S., Valcke, S., Beau, I.,
880   Alias, A., Chevallier, M., Déqué, M., Deshayes, J., Douville, H., Fernandez, E., Madec, G., Maisonnave, E.,
881   Moine, M. P., Planton, S., Saint-Martin, D., Chauvin, F. The CNRM-CM5.1 global climate model: description
882   and basic evaluation. *Climate Dynamics*, *40*(9–10), 2091–2121, https://doi.org/10.1007/s00382-011-1259-y,
883   2012

884   Winkelmann, R., Martin, M. A., Haseloff, M., Albrecht, T., Bueler, E., Khroulev, C., & Levermann, A. The
885   Potsdam Parallel Ice Sheet Model (PISM-PIK) – Part 1: Model description. *The Cryosphere*, *5*(3), 715–726,
886   https://doi.org/10.5194/tc-5-715-2011, 2011

887   Yukimoto S, Adachi Y, Hosaka M et al (2012) A new global climate model of the Meteorological Research
888   Institute: MRI-CGCM3—model description and basic performance. J Meteorol Soc Japan Ser II 90:23–64,
889   https://doi.org/10.2151/jmsj.2012-A02, 2012

890   Zheng, W., & Yu, Y. Paleoclimate simulations of the mid-Holocene and last glacial maximum by FGOALS.
891   *Advances in Atmospheric Sciences*, *30*(3), 684–698, https://doi.org/10.1007/s00376-012-2177-6, 2014

892   Zwally, H. J., Li, J., Robbins, J. W., Saba, J. L., Yi, D., & Brenner, A. C. Mass gains of the Antarctic ice sheet
893   exceed losses. *Journal of Glaciology*, *61*(230), 1019–1036, https://doi.org/10.3189/2015jog15j071, 2015

894